Electrochemical Fabrication of Multi-Nanolayers

12

Paul McCloskey, Terence O'Donnell, Brice Jamieson, Donald Gardner, Michael A. Morris, and Saibal Roy

Contents

P. McCloskey (✉)
Tyndall National Institute, University College Cork, Cork, Ireland
e-mail: paul.mccloskey@tyndall.ie

T. O'Donnell
University College Dublin, Dublin, Ireland
e-mail: terence.odonnell@ucd.ie

B. Jamieson
ELIX Wireless Charging Systems, Vancouver, Canada
e-mail: brice.jamieson@gmail.com

D. Gardner
Intel Corporation, Santa Clara, USA
e-mail: d.s.gardner@intel.com

© Springer International Publishing Switzerland 2016

M. Aliofkhazraei, A.S.H. Makhlouf (eds.), *Handbook of Nanoelectrochemistry*,
DOI 10.1007/978-3-319-15266-0_1

Abstract

The fabrication of multi-nanolayer structures can in some cases be achieved electrochemically if, for example, the plating current density has a significant effect on the deposit composition or if reverse plating changes the composition. Moreover, the realization of a multi-nanolayer structure can also crucially affect the properties of the material. This chapter will look at one material system in which both of the above apply, namely, amorphous Co-P.

When produced using conventional DC plating, amorphous Co-P tends to exhibit perpendicular magnetic anisotropy and hence very low permeability and somewhat high coercivity. This limits the usefulness of the material as a magnetic core for power conversion applications which require low coercivity, high saturation magnetization, high permeability, high anisotropy field, and high resistivity. Riveiro et al. used pulse reverse plating to fabricate multilayers of alternate magnetic and nonmagnetic materials. With the thickness of the magnetic layers at around 30 nm, they were able to achieve in-plane anisotropy and low coercivity 8 A m^{-1}.

This chapter will describe the early work and a selection of subsequent research on multi-nanolayers of amorphous Co-P, e.g., Perez et al., who used pulse plating, and McCloskey et al., who improved the saturation magnetization and thermal stability of the material.

Keywords

Electrochemical • High frequency soft magnetic material • Integrated inductor • Multi-nanolayer • Nanotechnology • Thermal stability Co–P

Introduction

The last 30 years have seen a revolution in the area of materials science centered around the development of solid structures with at least one dimension below 100 nm. These can be 3D materials with all dimensions below 100 nm (known as nanoparticles), 2D materials (essentially thin films), 1D materials (nanowires), and 0D materials with all dimensions below 10 nm, and often described as quantum dots [1]. It also encompasses materials which are nanostructured such as mesoporous or microporous substances that have structure arrangements of small pores [2]. The use of these materials in various fields is known as nanotechnology [3, 4], and while

M.A. Morris
University College, Cork, Ireland
e-mail: m.morris@ucc.ie

S. Roy
Tyndall National Institute, Cork, Ireland
e-mail: saibal.roy@tyndall.ie

Table 1 Summary of key nanotechnology references

Summary	Author/References
An overview of nanoparticle preparation and science	Karkare [1]
Details of nanoporous materials used as nanoparticle hosts	Hanrahane et al. [2]
Introduction to the theory of nanoscience and applications	Mansoori [3]
Basic introduction to nanotechnology and potential applications	Wilson et al. [4]
Perspective on the development of nanoscience	Lacaze [5]
Landmark paper detailing scaling development in microelectronics and Moore's Law	Moore [6]
Scaling and miniaturization in microelectronics	Roco and Gargini [7]
Roadmap for data storage requirements	Information Storage Industry Consortium [8]
Review of the emerging area of Spintronics for novel devices	Wolf et al. [9]

it is normally associated with hi-tech applications such as in the information and communications area, nanotechnology spans areas as diverse as biomedicine, transistors, and separation media. While there are many potential architects of the nanorevolution including Davy, Feynman, and Drexler [5], there is no doubt that the main driver of nanotechnology has been the microelectronics industry and the development of ultrasmall transistor devices. Scaling in the device industry (and, thus, our control of substrate features below 100 nm dimension) has been precipitated by an observation by Gordon Moore where he noted that the number of devices on a semiconductor chip doubled every 18–24 months [6]. Key references in nanotechnology are summarized in Table 1 below.

As dimensions have shrunk, miniaturization has not only been applied to silicon but also to a series of other materials including interconnects, vias, dielectrics, and photolithographic masks/resists [7]. One of the areas that have been as aggressively scaled as the silicon devices has been memory storage, which has needed to maintain commensurability because of the need to store an ever-increasing amount of information in both volatile and permanent formats [8]. Typical targets include 64 Tb storage capacities by around 2020 and magnetic feature volumes of less than 1500 nm^3 (although it is worth noting that dimension cannot be wholly stripped from the fundamental magnetic properties of the materials such as coercivity).

The global market for nanomagnetic materials and devices is growing markedly with sales expected to reach $9 billion by 2017. The data storage sector alone had sales of $6.9 billion in 2012, but markets are rapidly developing nanomagnet-based applications in sensors, biosensors, and bioassay platforms and should reach nearly $8.4 billion in 2017 while markets for sensors, biosensors, bioassay products, and giant magnetoresistance (GMR) readers are expected to develop quickly. Indeed, limitations in silicon technologies may precipitate the development of novel spintronic-based switches as devices [9]. Other markets for magnetic materials include soft magnetic cores, ferrofluids, catalysts, and environmental remediation products. It is worth stressing that there is no universal material for all these applications and any potential technology will be based around development of novel optimized systems that are likely to be unique for each application.

Electrodeposition

Electrodeposition can be applied to the fabrication of multi-nanolayers in which the composition is modulated. Such multilayer structures are of interest in relation to GMR [10], mechanical properties [11], and in some cases the improvement in soft magnetic properties [12, 13].

Modulation of composition can be achieved by either depositing the different components from separate electrolytes or by using voltage or current modulation to enable deposition from a single bath. A disadvantage with the former method is that it requires physical transport between electrolytes following the deposition of each layer. Whether or not it is possible to achieve composition modulation from a single bath depends on the particular properties of the electrochemical system being considered, and the circumstances in which it is possible will now be discussed.

The electrodeposition of a metal involves the reduction of metal ions in an electrolyte at a negatively charged cathode. As per Faraday's law, the amount of metal deposited is directly related to the quantity of charge transferred at the cathode and hence the current flowing. In the case of alloy plating, the amount of each component deposited will be proportional to the amount of charge transfer at the electrode, which is related to the deposition of each individual component of the alloy. Consequently, the composition of an alloy will be altered if the fraction of the overall current density related to a particular component is changed. Current flow in an electrodeposition process is driven by the voltage supplied, and hence it is necessary to consider the relationship between current and potential in an electrochemical electrode.

When a metal electrode is placed in a solution containing ions of the metal, an exchange equilibrium arises in which the number of metal atoms dissolving into the solution is equal to the number of metallic ions discharging and depositing on the electrode. As a result of this exchange, the electrode is at an equilibrium potential E relative to the solution. In order to drive the system away from equilibrium so that current can flow and metal will be deposited, the potential has to be changed to a new value $E(I)$, and the difference between these potentials is termed the "overpotential,"

$$\eta = E\left(I\right) - E \tag{1}$$

Electrodeposition always entails a number of steps, which include

- "Charge transfer," in which metal ions are neutralized and adsorbed
- "Mass transport," in which metal ions diffuse through a "stagnant" layer of electrolyte to the electrode surface
- "Incorporation," in which the adsorbed atom is incorporated into the growing lattice

The slowest step in the overall electrode reaction is rate determining. However, several of the steps can have low reaction rates and hence can contribute to the

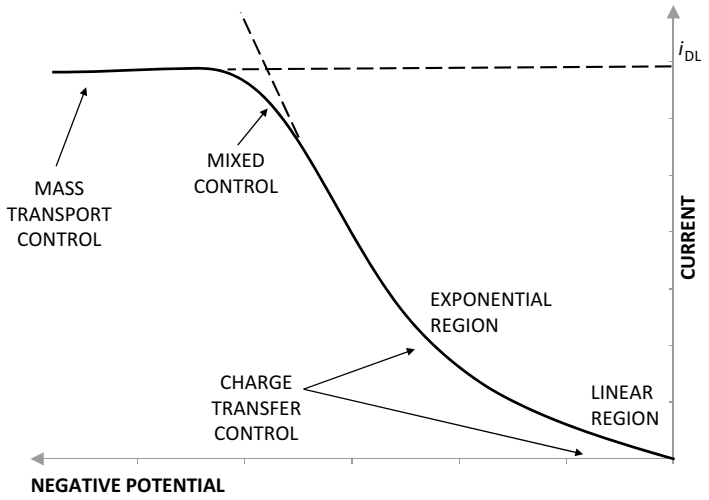

Fig. 1 Schematic of current density versus potential for electrodeposition

overall electrode reaction rate. The only stage that is directly affected by the electrode potential is charge transfer. The relationship between current density and potential for electrodeposition is illustrated schematically in Fig. 1.

It can be seen that initially potential has a strong influence on the linear and exponential regions in which the deposition is under "charge transfer" control. However, as the potential is increased further, "mass transport" begins to influence and eventually dominate the reaction rate, at which point the potential has no influence on current density. The exponential region applies to large values of overpotential, e.g., for a cathodic process, $\eta >= -100$ mV [14]. By taking logarithms, this region can be represented by the linear Tafel relationship for reduction shown below:

$$\eta = a - b \log |i| \tag{2}$$

The effect of changing the overpotential on the composition of an alloy can be understood by considering the Tafel plots for a two-component alloy x-y shown in Fig. 2.

The logarithm of the ratio of the current densities for each component is a measure of the alloy composition, and for an overpotential η, this is given by

$$\ln\left(i_x / i_y\right) = \ln\left(i_x\right) - \ln\left(i_y\right) \tag{3}$$

with

$$\ln\left(i_x\right) = a_x + b_x \eta \tag{4}$$

and

$$\ln\left(i_y\right) = a_y + b_y \eta \tag{5}$$

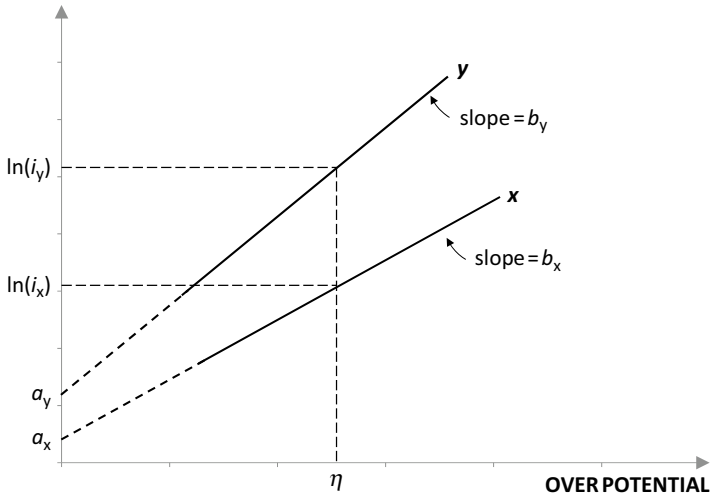

Fig. 2 Schematic Tafel plots for deposition of alloy x-y

Hence, substituting into Eq. 3, we obtain

$$\ln\left(i_x / i_y\right) = \left(b_x - b_y\right)\eta + a_x - a_y \tag{6}$$

It can be seen from Eq. 6 that the composition of the alloy will be unchanged by changes in overpotential (η) if the Tafel slopes of each component are identical ($b_x = b_y$).

The above argument applies to a situation in which the reaction rate for both components is under charge transfer control. However, if one of the components is under mass transfer control, then changing the value of overpotential will change the composition. Formulating the electrolyte to contain a low concentration of a more noble metal and a high concentration of a less noble metal can create this situation. Ions of the more noble metal will be quickly depleted at the cathode, and consequently its deposition will be under mass transport control. Composition modulation is achieved by varying the overpotential between a value at which only the more noble metal deposits and a value in which both metals deposit with the less noble metal being deposited under charge transfer control. The layers thus produced will alternate between pure noble metal and a low concentration of noble metal. This approach has been applied to the fabrication of multilayers of Cu-Ni [15], Ni-Fe-Cu/Cu [16], and Co/Cu [17].

An implicit assumption in the use of Tafel plots to determine the effect of overpotential on alloy composition is that the deposition of one component is unaffected by the presence of other alloy components. Often this is not the case, a situation described by Landolt [18] as "charge transfer coupled," i.e., the partial currents are not independent of each other. Landolt [18] further categorized such systems as either "inhibited codeposition" or "catalyzed codeposition."

One of the situations in which this arises is the electrodeposition of amorphous alloys based on iron group metals (Fe, Co, Ni). Amorphous alloys of these metals

can be produced by the codeposition of P or B. In aqueous solution, P and B cannot be deposited alone but can readily be deposited in the presence of iron group metals, a phenomenon usually termed "induced codeposition." The overpotential does often seem to affect the composition, as many studies have indicated a tendency for the deposited alloy to become more rich in the iron group metal as the current density is increased; e.g., this was the case for Ni-P, Co-P and Ni-Co-P [19], Co-P [13], and high phosphorous bath content Ni-P [20]. Perez et al. [13] used this dependency of composition on current density to produce modulated Co-P films with alternate high and low P contents.

Pulse reverse plating involves reversing the polarity of the cathode and anode during part of the plating cycle. During the "reverse" period, material previously deposited will dissolve back into solution. In the case of an alloy, pulse reverse plating can be used to produce composition modulation if one of the alloy components has a greater tendency to dissolve than other components. This is the case for Co-P plating as the Co tends to dissolve more quickly than P during current reversal. Riveiro and Riveiro [12] used this effect to produce nanolayered deposits.

Magnetic Property Overview

Fundamentally, magnetism is defined by both the spin and orbital momentum of electrons, and since most solid materials contain many electrons within an effectively continuous band structure, permanent magnetism is actually rather rare [21, 22]. However, all bulk or molecular materials can be magnetically categorized according to a limited number of forms. These are summarized in Fig. 3.

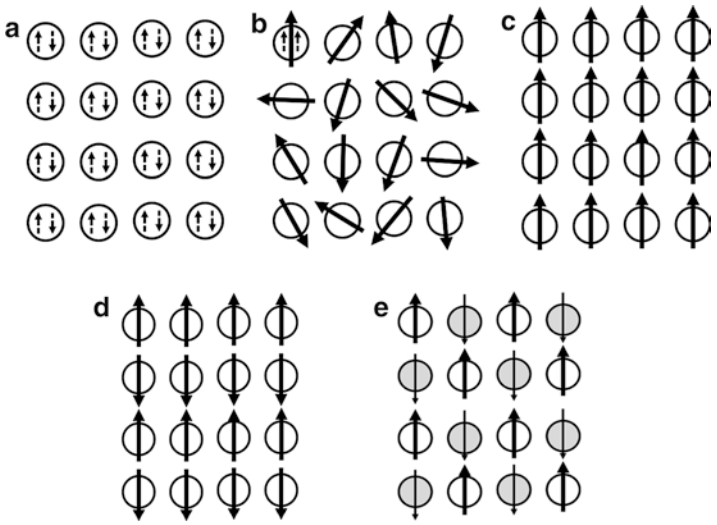

Fig. 3 Types of magnetism illustrated schematically. Electrons spins are indicated as dashed arrows and magnetic moment of individual atoms as a large arrow

Diamagnetism (Fig. 3a) is exhibited in materials where all of the electrons are paired and the total magnetic moment is essentially zero (at all temperatures above 0 K). Paramagnetic materials contain atoms, molecules, or ions that have unpaired electrons, but within the solid and in the absence of a magnetic field, these individual entities behave independently and show no tendency for the magnetic moments to align (Fig. 3b). In an applied field, a net magnetic moment will develop because of field-imposed alignment. In a few special cases, alignment of the individual magnetic moments spontaneously occurs, and a ferromagnet results (Fig. 3c). In iron, e.g., this occurs because the band structure is such that spatial minimization of electron–electron repulsions is more significant than the energy decrease defined by electron pairing. In the vast majority of examples, neighboring atoms/molecules containing unpaired electrons will antiferromagnetically align (maximizing attractive north–south low-energy arrangements, minimizing the repulsive arrangements). These are called antiferromagnets and have close to zero magnetic moment (Fig. 3d). A few special cases exist where even though the system is antiferromagnetically arranged, because of the presence of heteroatoms of differing magnetic moment, the total magnetic moment is nonzero, and these materials are called ferrimagnetic (Fig. 3e).

In Fig. 3e, heteroatoms are shown as filled circles, and these carry a smaller net moment indicated by the thinner arrow.

Bulk ferromagnets and ferrimagnets are characterized by strong magnetic moments below a critical temperature known as the Curie temperature for ferromagnets and the Néel temperature for ferrimagnets. Above these temperatures, the materials are paramagnetic because of thermal randomization of electron spins.

When a ferromagnetic material is placed is a magnetic field, H (the magnetizing field), an extra field is induced within the magnetic material as the unpaired electrons in the material align in response to H. This field, B, is referred to as the magnetic induction or, more commonly, the magnetic flux density and arises from the properties of the material itself. In SI units, the relationship between these fields is usually expressed as

$$B = \mu_0 \left(H + M \right) \tag{7}$$

where $\mu_0 = 4\pi \times 10^{-7}$ H m^{-1}, B is in teslas, H and M are both in A m^{-1}, and B, H, and M are all vector quantities.

This expression shows that the B field induced in the material is proportional to the sum of the magnetizing field H and a magnetization, M, arising from the material itself. The constant of proportionality is the permeability of free space.

Alternatively, the B field is often expressed in a direct relationship to the magnetizing field H as

$$B = \mu_0 \mu_r H \tag{8}$$

where μ_r is the relative permeability, a value representing the strength of the response of a magnetic material to an applied field. Materials with a higher permeability will respond more strongly to a given field than materials with a low permeability.

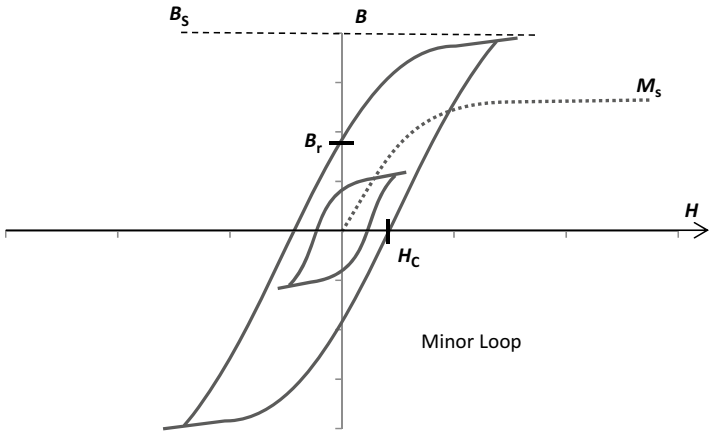

Fig. 4 Typical *B-H* curve for a ferromagnetic material

In general, the relationship between *B* and *H* in a ferromagnetic material is highly nonlinear and hysteretic, taking the form of a *B-H* curve. A typical example of such a curve is shown in Fig. 4. Moreover, the exact value of *B* arising within a magnetic material from application of an *H* field is dependent on the previous history of magnetization of the material.

The magnetization curve for any material is typically characterized in terms of the parameters shown in the figure, i.e., the saturation flux density, B_s, the remnant flux density, B_r, and the coercivity, H_c. In soft magnetic materials, the slope of the *B-H* curve, i.e., the permeability, can be an important consideration. A specific application of magnetic materials might demand *B-H* curves of a specific shape, and therefore material development efforts usually focus tailoring the shape of the *B-H* curve using different alloy compositions, production, or processing techniques. In order to appreciate the cobalt phosphorus material development described later in this chapter, it is important to explain some of the underlying processes which give rise to the shape of the *B-H* curve.

The magnetization curve of ferromagnetic materials is understood in terms of the "molecular field" theory advanced by Pierre Weiss in 1906 [23]. Weiss postulated that a ferromagnet in an unmagnetized state is spontaneously divided into a number of small regions called "domains." Each domain is spontaneously magnetized to the saturation value M_s, but the directions of magnetization of the domains are all different such that in a large collection they cancel and the sample has no overall magnetization. Consequently, the process of magnetization may be understood as changing the specimen from a situation in which there are many misaligned domains to a situation where all the domains are aligned with the direction of the external applied magnetic field *H*. At this point, the sample has reached its saturation value, M_s or B_s.

This transformation from misaligned domains to fully aligned domains takes place by two mechanisms, namely, domain wall motion and domain rotation.

Domain wall motion allows domains that are favorably aligned with the external field to grow in size. This process can involve both reversible and irreversible steps. Domain walls can be pinned or impeded from moving by nonmagnetic inclusions in the materials. When a domain wall becomes unpinned, it advances in a sudden step known as a "Barkhausen jump." Such events are irreversible and are a cause of hysteresis and consequently energy loss. Nevertheless, domain wall motion typically requires less energy than domain rotation and so tends to dominate the magnetization process at low fields where the magnetization curve has the steepest slope; i.e., a small change in field produces a large change in magnetization. At higher fields, the slope of the magnetization curve is reduced (and hence a relatively large change in field is required to produce a small change in M). This is generally the point at which there are few favorably aligned domains left to grow in size and so further magnetization takes place by domain rotation where the magnetization of unaligned domains rotates to align with the magnetic field.

Magnetic materials may be anisotropic, in which there is an easy-axis direction in which it is "easy" to magnetize the material and a hard-axis direction in which it is "hard" to magnetize – see Fig. 5 for schematic B-H loops of an anisotropic material.

The direction and strength of the anisotropy will be determined by various contributions to anisotropy which can arise from a number of sources, namely, the

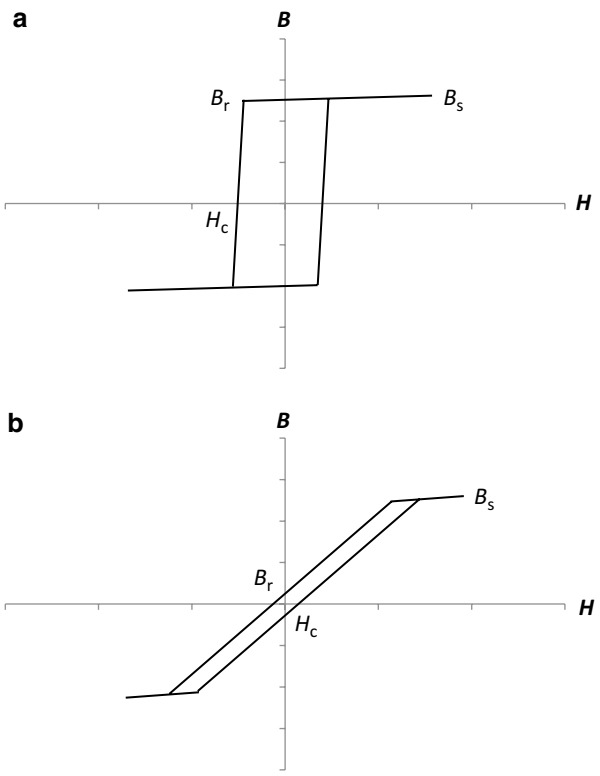

Fig. 5 Schematic B-H loops of anisotropic material, (**a**) Easy axis, (**b**) Hard axis

magnetocrystalline anisotropy, the magnetoelastic anisotropy, the shape anisotropy, and the induced anisotropy. Of these, only the magnetocrystalline anisotropy is intrinsic to the material. It acts as a force that tends to hold the magnetization in certain equivalent crystallographic directions and is mainly due to spin–orbit interactions [24]. The magnetoelastic anisotropy results from stress in the film. Shape anisotropy arises from the fact that for a nonspherical open magnetic circuit specimen, a demagnetizing field will arise from induced magnetic poles at the surfaces of the sample, the strength of which is inversely proportional to the length of the axis. On the shortest axis of a sample, the demagnetizing factor is the strongest. Thus, shape anisotropy will favor the formation of an easy axis along the longest axis of a material sample and will generally force the easy axis to lie in the plane of a thin film as opposed to perpendicular to the film. In the plane of a finite film as well, the shape anisotropy will push the easy axis to lie along the longest possible axis.

The easy axis is the direction in which the material can be brought to saturation with the lowest applied field, which also implies that the slope of the *B-H* (and hence the relative permeability) is highest in this direction as can be seen illustrated in Fig. 5a. Conversely, as shown in Fig. 5b, the permeability would be expected to be lowest in the hard-axis direction.

As previously mentioned, domain wall movement entails energy loss through irreversible Barkhausen jumps. In addition, such jumps dissipate energy due to the formation of microscopic eddy currents in the region of the domain wall. As a result, magnetization through domain wall movement tends to be effective only up to moderate frequencies, e.g., 10–100 kHz [25], and indeed permeability in the easy axis typically decreases rapidly with frequency.

In contrast, magnetization through rotation, especially if domains are oriented perpendicular to the applied field, occurs gradually and uniformly throughout the material and can be almost lossless. As a result, although the permeability in the hard axis is lower, it remains more stable with frequency. This is the primary reason why anisotropy is often deliberately induced in the magnetic core of magnetic devices designed for high-frequency operation.

It should be pointed out that for conductive magnetic materials, used in the hard axis, there will still be macroscopic eddy currents induced by the flux changes, as would be expected from any conductor experiencing a time-changing magnetic field. Such macroscopic eddy current loss is a major loss mechanism in magnetic materials at high frequencies and provides the main motivation for the development of higher-resistivity materials.

As mentioned above, shape anisotropy would generally dictate that for thin films the easy axis would lie in the plane of the film. However, in some materials, with, for example, strong crystal anisotropies, it may be energetically favorable for the easy axis to lie perpendicular to the plane of the film. Such films are said to have perpendicular anisotropy, which can lead to the formation of "stripe domains," which consist of alternate antiparallel domains, leading to poor in-plane soft magnetic properties, i.e., very low permeablity and the requirement for high external fields (>800 A m^{-1}) to reach saturation [26].

The above describes the magnetic properties largely in terms of the macroscopic perspective of magnetic domain interaction. However, when dealing with materials on the nanoscale, it is also necessary to realize that the fundamental magnetic properties of a material can change dramatically with dimension. Since magnetic properties derive from correlated movements of electronic charge, changes in electronic band structure, crystallography, the contribution of surface states and morphological variation can cause dramatic changes in magnetism with dimension.

For example, groundbreaking work by Louise Néel [27] led to the identification of a new form of magnetization (superparamagnetism) which appears when the size of the particles is such that a single domain exists in the whole solid [28]. Effectively, this is at particle dimensions of less than 50 nm dependent on the material. Usually, nanoparticles have a preferred direction for magnetic alignment (called uniaxial anisotropy); however, the magnetic alignment direction will periodically "flip" or rotate due to thermal motion. When the particles are flipping rapidly, within a real time, the net magnetic moment of the nanoparticle is effectively zero. This is said to be the superparamagnetic state. In this state, an external magnetic field is able to "magnetize" the nanoparticles via spin rotation similar to the magnetization of a collection of paramagnetic molecules. However, their magnetic susceptibility is much larger than a conventional paramagnet.

State of the Art for Electroplated Soft Magnetic Alloys

There has been a significant level of research interest, mainly driven by the demand in various microelectronic applications, in developing high-performance soft magnetic alloys that exhibit good properties, i.e., the coercivity (H_c) should be minimized, especially in the hard axis, the saturation flux density (B_s) should be maximized, as should resistivity (ρ) so as to minimize eddy current loss.

One of the first significant developments in this area introduced by IBM in 1979 [29, 30] was the electrodeposition of permalloy ($Ni_{81}Fe_{19}$) (Bs = 1.0 T, $\rho = 2.8 \times 10^{-7}$ Ωm and H_C = 72 Am^{-1}), for application as the core material of a thin-film inductive head to increase magnetic recording density. The introduction of magnetoresistive read head by IBM in 1991 resulted in the need of high-speed writing head with a very narrow writing track width and the capability of recording in a highly coercive recording media to achieve a higher density of recording. This has led to the advent of newer permalloy compositions such $Ni_{45}Fe_{55}$ [31, 32] with better soft magnetic properties (B_s = 1.4–1.6 T, ρ = 4.0–4.5 × 10^{-7} Ωm and HC = 103 Am^{-1}). However, $Ni_{45}Fe_{55}$ films were particularly sensitive to residual stresses, whereas $Ni_{80}Fe_{20}$ films were not, due to its ultralow magnetostriction (<1 × 10^{-6}) value.

Osaka [33] produced electroplated films of CoNiFe with sulfur-containing additives such as saccharin and thiourea. It was found that with sulfur content at 0.9 % the resistivity had increased to 5.1 × 10^{-7} Ωm with a reasonable saturation flux density of 1.7 T, low coercivity of 72 Am^{-1}, and permeability retained up to 30 MHz frequency.

Electrodeposited amorphous Co-P alloys have reported values of coercivity that are extremely low, i.e., $H_c < 24$ A m^{-1}, even at high values of resistivity, i.e., $\rho = 1.9 \times 10^{-6}$ Ω m [34]. However, Co-P has a strong tendency to form an out-of-plane, perpendicular anisotropy, and electrodeposition techniques must be employed that prevent this by producing a multi-nanolayer structure.

Such electrodeposited magnetic materials are an attractive possibility in the integration of on-chip inductors into silicon process technology, which has been a major challenge in the development of monolithic solutions for wireless communications, RF ICs, radar, power delivery, and EMI noise reduction [35]. The use of such materials has the potential to considerably reduce the footprint required but requires a material with low losses at high frequency.

Early Work on Electrodeposited Co-P

DC Plated Co-P

Riveiro and Sanchez-Trjillo [26] investigated the anistropy behavior of electrodeposited amorphous Co-P films. They used a plating bath which was based on those described by Brenner et al. [20], which for a "high" phosphorous deposit of 9–11 % had a bath composition and conditions as shown in Table 2.

As a substrate for plating, Riveiro and Sanchez-Trjillo [26] used smoothed polycrystalline copper. *M-H* hysteresis loops of the samples thus produced were obtained using two methods, the integrating fluxmeter and the transverse magneto-optic Kerr effect (MOKE). The ratio of remnant magnetization to saturation magnetization M_r/M_s as obtained by these methods is shown plotted against deposit thickness in Fig. 6.

It can be seen that for samples with a thickness below 400 nm the value of M_r/M_s is high (which implies a high permeability) but as the thickness is increased the value of M_r/M_s, decreases (which implies a low permeability). Riveiro and Sanchez-Trjillo [26] interpreted these results as indicating that an in-plane anisotropy is present for samples with a thickness below 400 nm but as the thickness is increased above 500 nm the anisotropy develops an out-of-plane direction eventually becoming perpendicular at approximately 10 μm.

Table 2 Plating bath composition and conditions

Component	Amount (g l^{-1})
H_3PO_3	40
Co CO_3	~15 (sufficient to achieve desired pH)
$CoCl_2.6H_2O$	180
H_3PO_4	50
Temperature (°C)	75–95
Current Density (A m^{-2})	500–4000
PH	0.5–1.0
Anode	Co

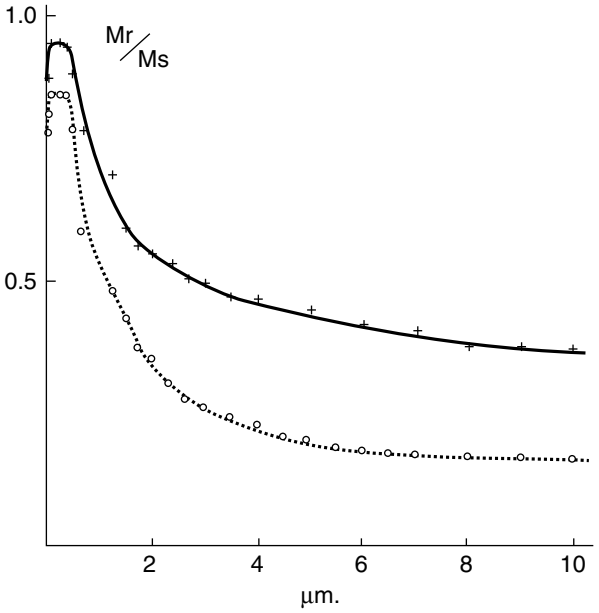

Fig. 6 Ratio of M_r/M_s, versus sample thickness with; "0" indicating "Integrating fluxmeter" and "+" indicating "Kerr effect" (Reproduced from Riveiro and Sanchez-Trjillo [26])

This phenomenon was explained based on the theory presented by Chi and Cargill [36] that the anisotropy is due to the formation of a "columnar structure" which arises due to fluctuations in the composition. However, a detailed study by Ruythooren et al. [37] of DC-plated Co-P films using transmission electron spectroscopy (TEM) failed to find evidence of a columnar microstructure.

Pulse Reverse Plated Co-P

Riveiro and coworkers investigated the use of pulse reverse plating to produce composition-modulated films and hence interrupt the "presumed" columnar growth. Initially, this was achieved by adding a 5 Hz sinusoidal current to the conventional DC electrodeposition current [34]. Subsequently, Riveiro and Riveiro [12] used a square wave with current reversal – see Fig. 7.

They used the following settings:

- Forward current density, $CD_{\text{forward}} = 5000$ A m^{-2}
- Reverse current density, $CD_{\text{reverse}} = 2000$ A m^{-2}
- Forward on-time $t_{\text{forward}} = 90$–500 ms
- Reverse on-time $t_{\text{reverse}} = 50$ ms

The plating bath composition was very similar to that shown in Table 2 except that the H_3PO_3 was higher at 65 g l^{-1}.

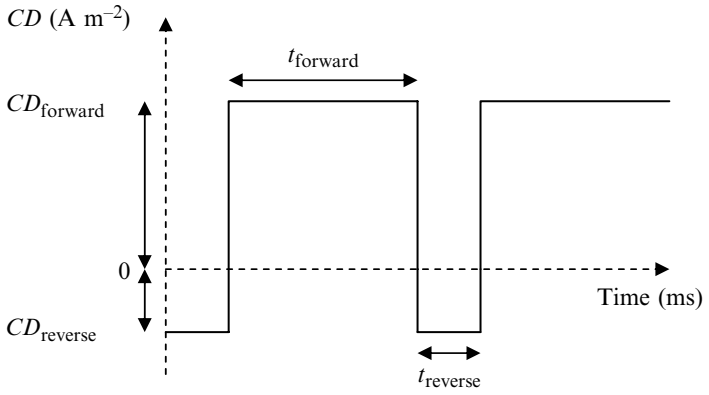

Fig. 7 Pulse Reverse Waveform used by Riviero et al. [12]

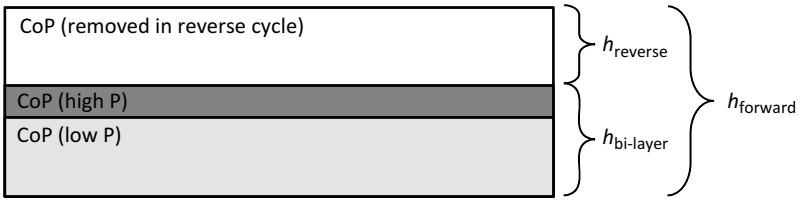

Fig. 8 Effect of Pulse Reverse waveform

It was supposed by Riveiro et al. [12] that during the forward on time, $t_{forward}$, Co-P is deposited (with a thickness of $h_{forward}$) while during the reverse time, $t_{reverse}$, Co-P is removed (with a thickness of $h_{reverse}$). During the reverse cycle, Co is removed preferentially, and hence the upper part of the remaining layer is enriched in P.

Consequently, a bilayer structure is created, which is represented in Fig. 8.

Using this approach Riveiro and Riveiro [12] fabricated multilayers of alternate magnetic and nonmagnetic materials. The magnetic layers had a composition of $Co_{76}P_{24}$ while the nonmagnetic layers had a composition of $Co_{67}P_{33}$ (thickness 2–5 nm).

Holding the thickness of nonmagnetic layers constant, they varied the thickness of the magnetic layers. They found that the H_c initially fell from 40 A m^{-1} (at a magnetic layer thickness of 3 nm) to 8 A m^{-1} (at a magnetic layer thickness of 30 nm). Above this thickness, the H_c started to rise again, and "stripe domains" were observed when the magnetic layer thickness was greater than 150 nm. Riveiro et al. [40] made a thorough study of magnetic domains in multilayered amorphous Co-P alloys produced by pulse reverse plating.

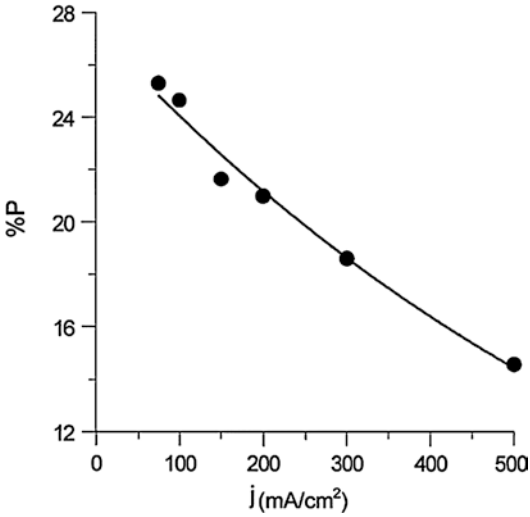

Fig. 9 Co-P composition versus electrolytic current density (Reproduced from Perez et al. [13])

Pulse Plated Co-P

The effect of DC plating current density on the deposit composition of Co-P was investigated [13]. It was found that the composition is strongly dependent on current density as is shown in Fig. 9.

Perez et al. [13] went on to exploit this effect by using square wave pulse plating at different current densities to produce multilayer structures in which both layers were ferromagnetic and where the composition of the first layer was $Co_{83}P_{17}$, the composition of the second was $Co_{78}P_{22,}$ and the double layer thickness was in the range 10 nm to 30 μm. These layers were replicated in order to produce a stack of layers with alternating composition. Perez et al. [13] did not quote the exact plating conditions used in this study but in subsequent work aimed at fabricating a fluxgate sensor with an electrodeposited amorphous Co-P core [38], described using [39] a single electrolyte and current densities of 5000 and 1000 A m^{-2} to modulate the composition of the layers. The plating waveform utilized is shown in Fig. 10.

In their initial study, Perez et al. [13] experimented by varying the bilayer thickness while keeping a constant total deposit thickness of 30 μm. They found that they could reduce the normalized perpendicular anisotropy of the film from 1 (bilayer thickness of 30 μm) to 0.38 (bilayer thickness of 10 nm).

Subsequently, Perez et al. [13] tried keeping the number of bilayers constant at 1000 while varying the composition of the layers. They found that the perpendicular anisotropy could be related to the difference between the B_s of the two layers that form a bilayer. With a difference in B_s smaller than 0.3 μ_B $atom^{-1}$ (resulting from a difference in current density smaller than 3000 A m^{-2}), the normalized perpendicular anisotropy was reduced from 1 to 0.25.

The bilayer films were characterized, and it was found that they exhibited the magnetic properties, H_c = 3–10 A m^{-1}, B_s = 0.6 T, and permeability, $\mu = 10^4$.

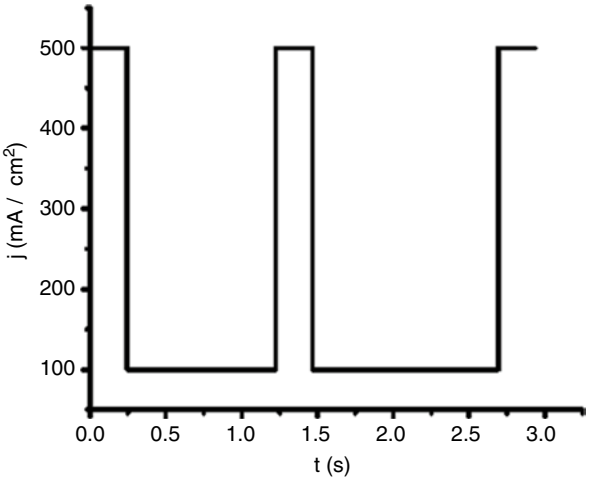

Fig. 10 Plating waveform used to fabricate multilayer Co-P core for fluxgate sensor (Reproduced from Perez et al. [38]])

Bitter domain pattern analysis was carried out, and it was found that domain walls were present and that these were associated with more than one layer, thus indicating exchange coupling between layers. Perez et al. [13] contrasted this with a similar bitter analysis of magnetic/nonmagnetic layers carried out by Riveiro et al. [39], in which Neel and Cross-Tie walls were observed, indicating that there was no exchange coupling between the ferromagnetic layers. Based on this difference, Perez et al. [13] suggested that the presence of exchange interaction between the ferromagnetic bilayers was the reason for the lower coercivity values exhibited.

Electrodeposited Co-P With Higher Saturation Magnetization

Background

As discussed earlier, Riveiro and Riveiro [12] produced thick films of amorphous Co-P with low coercivity using pulse reverse plating to fabricate multi-nanolayers of alternate magnetic and nonmagnetic material. The value of saturation magnetization B_s was not reported, but considering the composition and thickness of the magnetic layers it would be expected that the films would have saturation below 0.5 T.

As also discussed previously, Perez et al. [13] produced multi-nanolayers of amorphous Co-P using square wave pulse plating at two current densities. They produced multilayer structures which exhibited coercivity H_c = 3–10 A m^{-1}, saturation magnetization B_s = 0.6 T, and relative permeability μ_r = 10,000.

However, one of the key requirements for a material to be suitable for integrated inductors in a power delivery application is to have a high saturation magnetization coupled with a relatively high anisotropy field. In order to obtain a material with a higher saturation and high anisotropy field, it was decided to investigate the use of

a bath with lower phosphorous acid content than that used by Riveiro and Riveiro [12] and to optimize the plating waveform in order to obtain the best properties with the lower phosphorous bath.

Experimental

A bath was prepared with a composition similar to that shown in Table 2. The bath composition was identical to the bath used by Riveiro and Riveiro [12] except that the quantity of H_3PO_3 was reduced from 65 g l^{-1} to 30 g l^{-1}.

The cathode for the plating experiments was a silicon wafer with a top layer of 500 nm of silicon oxide and a conductive seed layer consisting of 20 nm titanium and 200 nm copper. All samples were plated in the presence of a uniaxial magnetic field of around 16 kA m^{-1}, which was provided using two large permanent magnets (140 × 100 × 100 mm) that were separated by a distance of 220 mm. The magnetic field was oriented to be parallel to the surface of the cathode. Cobalt metal pieces, in close contact with an inert Pt/Ti mesh, were used as the anode.

The film resistance was measured using the four-probe method in the central area of the wafer before and after plating. After dicing to the appropriate sample sizes, DC magnetic characterization was obtained using an ShB Instruments MESA-200 Magnetic Measurement System, and complex permeability spectra were measured using a Ryowa PMM9G1 permeameter. Compositional analysis was obtained using EDX.

The Brenner [39] bath does not work well if the pH is too high because under these conditions a powdery nonmetallic film is deposited. Moreover, the pH tends to rise with use, and hence, a low pH value is usually maintained with the addition of H_3PO_3. However, as this is the main phosphorus source and the aim was to reduce the phosphorus content, it was decided that HCl would be used to acidify the bath.

The trial consisted of two separate experimental runs, Run A and Run B.

Run A had a starting pH (i.e., no HCl added) of 1.7 while Run B had a starting pH of 1.4. Within each run, two sets of samples were produced. For the first set, the pulse parameters were kept constant and the pH of the bath was lowered by the addition of HCl. A pulse reverse waveform as shown in Fig. 11 was used. Apart from the presence of an off-time t_{off}, this waveform is very similar to that used by Riveiro and Riveiro [12] as shown in Fig. 7.

For the first set of samples, the pulse parameters were maintained as follows:

- Forward on time, $t_{forward}$ = 870 ms
- Forward current density, $CD_{forward}$ = 1700 A m^{-2}
- Reverse on time, $t_{reverse}$ = 54 ms
- Reverse current density, $CD_{reverse}$ = 670 A m^{-2}
- Off time, t_{off} = 72 ms

In the second set of samples, the pH was maintained at a constant value of around 0.88 and the forward on time $t_{forward}$ was varied between 96 ms and 5000 ms with the other pulse parameters kept as constant as possible.

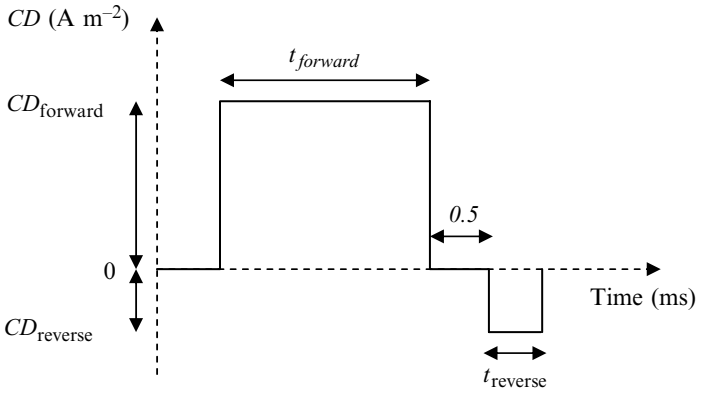

Fig. 11 Pulse Reverse Waveform used by McCloskey et al. [41]

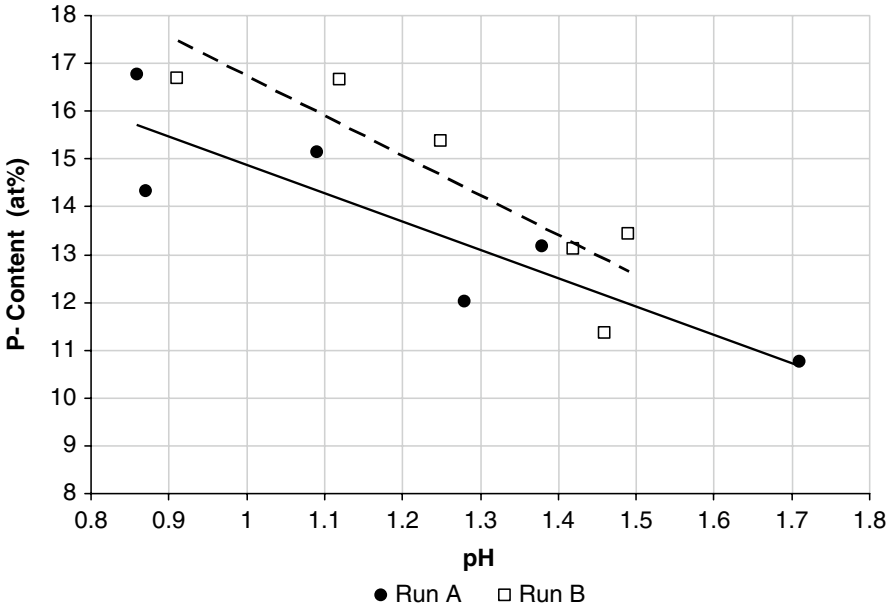

Fig. 12 Effect of pH on at.% P in deposit (Reproduced from McCloskey et al. [41])

Results and Discussion

Effect of pH (With Pulse Parameters Kept Constant)

At higher pH values (1.7–1.3), a "powdery" nonmetallic material was deposited particularly at the edges of the wafer. The size of the area affected by the nonmetallic deposit decreased dramatically as the pH was reduced and disappeared completely for pH values below about 1. The starting pH value influenced the phosphorus content of the deposit as is shown in Fig. 12.

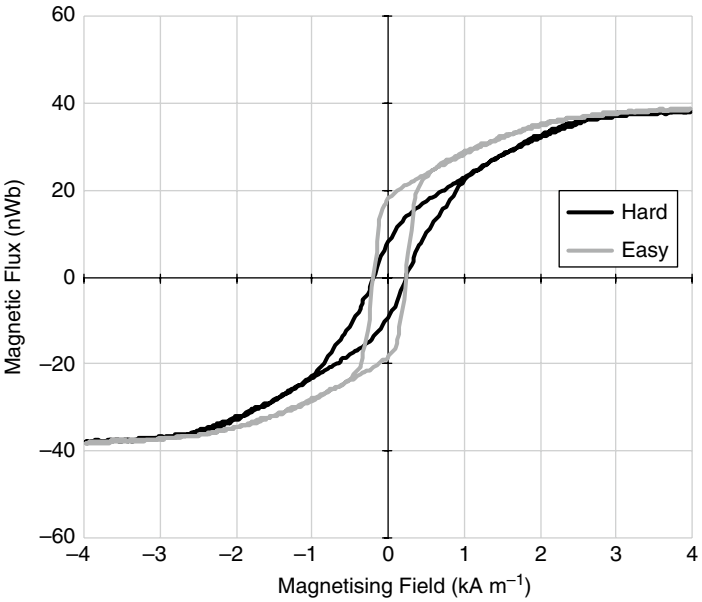

Fig. 13 Magnetisation loop of sample from Run A, Set 1 with pH = 1.7

Magnetization loops showed the samples to be magnetically soft with low values of H_c (i.e., below 40 A m^{-1}) for all samples except the starting sample of Run A – Set 1 (H_c = 263 A m^{-1}). This sample had the largest nonmetallic deposit. The magnetization plot for the starting sample of Run A is shown in Fig. 13. This loop shows three distinct regions that are characteristic of perpendicular anisotropy. That is, at applied fields below ~0.3 kA m^{-1}, the loop exhibits a large hysteresis (i.e., wide coercivity) followed by a region in which the magnetization is changed by the applied field but with little or no hysteresis and finally a region in which the magnetization is not changed by the applied field, i.e., the magnetization has reached saturation. Furthermore, the sample shows only rather small in-plane anisotropy. The easy axis, which exhibits the highest slope, i.e., a high permeability, was obtained at the orientation of the sample relative to the magnetic field applied during electrodeposition. The hard axis, which exhibits a lower slope, i.e., a lower permeability, was obtained at an orientation perpendicular to the easy axis.

An example of the much-improved magnetization loops obtained for samples plated at a lower pH is shown in Fig. 14. The magnetization plot consists of only two regions, i.e., a low-hysteresis region, in which the magnetization is changed by an applied field, and a further region in which the magnetization is unchanged by the applied field, i.e., the magnetization has reached saturation. This type of loop is typical for in-plane anisotropy.

Furthermore, the magnetization loop shows a pronounced anisotropy with a clear difference between the easy and hard axis.

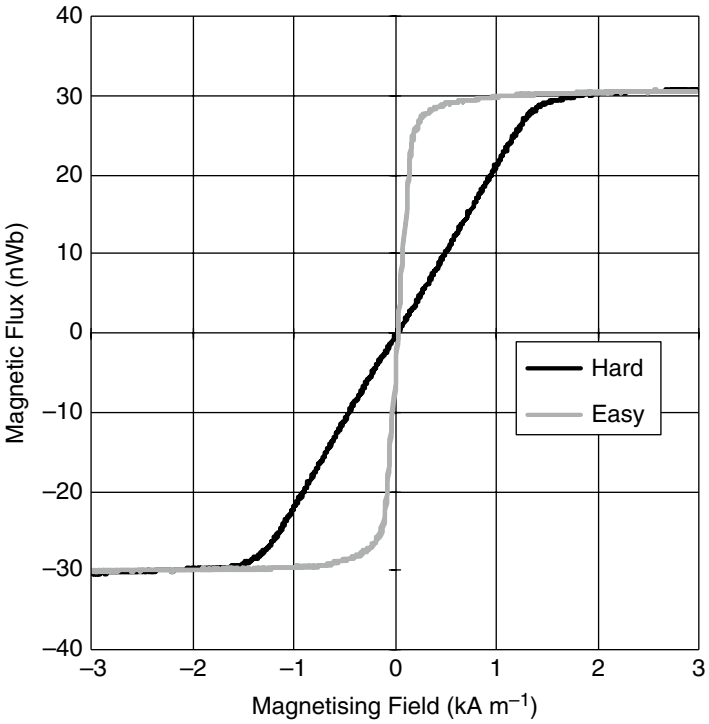

Fig. 14 Magnetisation loop of sample from Run A, Set 1 with pH = 1.28

The field required to rotate the magnetic orientation of the sample from the easy to hard axis orientation is known as the anisotropy field, H_k. On a B-H loop, it is the nonzero field at which the extrapolated hard axis loop intersects the easy axis loop. From Fig. 14, it can be seen that $H_k \sim 1.4$ kA m^{-1}.

The hard axis coercivity is plotted against pH for both Run A and Run B (excluding the results for samples produced with pH = 1.7) in Fig. 15. It may be seen that for both Run A and Run B, the H_c shows a downward trend with increasing pH.

It should be noted that for a given pH Run A has a lower % P but a higher H_c and hence the correlation of H_c with pH is not explained as simply a dependence on P content.

The saturation magnetization B_s is plotted against phosphorus content in Fig. 16 for both Run A and Run B. This is with the pulse plating parameters held constant and pH varied.

It can be seen that as anticipated the B_s increases with decreasing phosphorus content for both experimental runs, varying from 0.9 to 1.2 T.

Effect of Forward on Time (With pH Kept Constant)

As discussed earlier, Riveiro and Riveiro [12] used pulse reverse plating to create a bilayer structure of alternate compositions (see Fig. 8) and supposed that during the

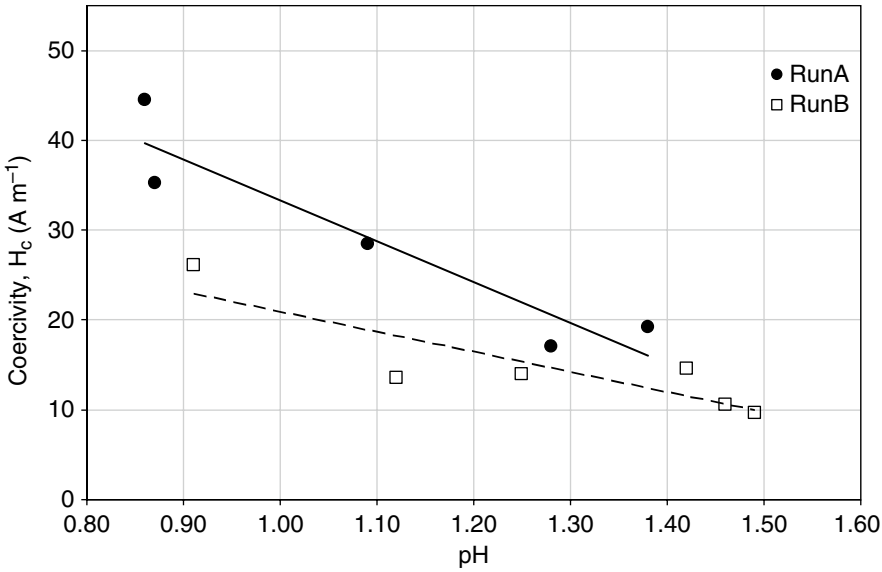

Fig. 15 Hard axis H_c versus pH for Set 1 samples (Reproduced from McCloskey et al. [41])

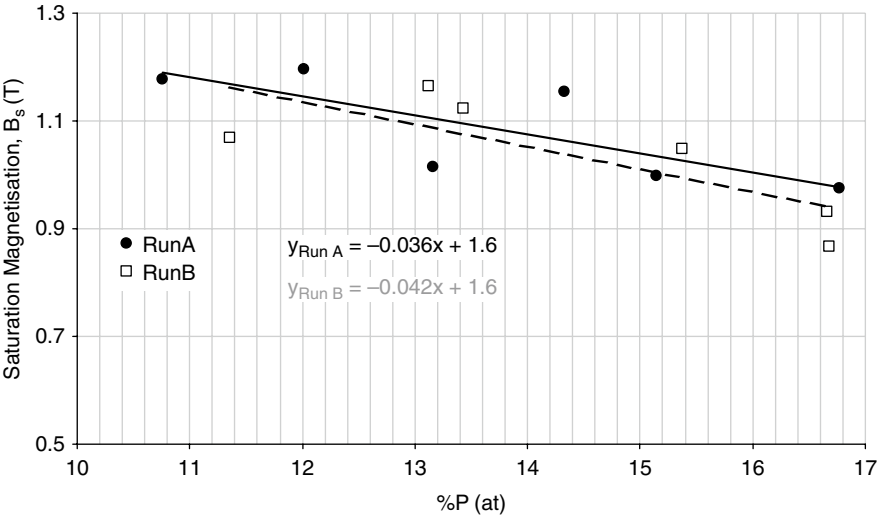

Fig. 16 Saturation magnetization B_s versus phosphorous content (Reproduced from McCloskey et al. [41])

reverse time Co is removed preferentially and hence the upper part of the deposit is enriched in P.

In a treatment similar to that in Riveiro and Riveiro [12] for a constant forward current density CD_{forward}, reverse current density $CD_{\text{reverse,}}$ and reverse time $t_{\text{reverse,}}$ the thickness of the bilayer is given by

$$h_{\text{bi-layer}} = kt_{\text{forward}} - h_{\text{reverse}} \tag{9}$$

where t_{forward} = forward on time and k is a constant. This thickness may be readily determined since it is also given by

$$h_{\text{bi-layer}} = \left(t_{\text{cycle}} / t_{\text{plating}}\right) h_{\text{sample}} \tag{10}$$

where t_{cycle} = total cycle time, t_{plating} = total plating time, and h_{sample} = sample thickness.

When the bilayer thickness is plotted against forward on time for each experimental run, a straight line with a negative intercept is obtained as shown in Fig. 17. The plots would show a zero intercept if no material was removed during the reverse cycle, and the value of the intercept is the average thickness of material removed during each reverse cycle. It will be noted that the intercept values are similar for both experimental runs (A and B).

The *B-H* loops obtained for the samples showed that the hard axis H_c was strongly influenced by t_{forward} (see Fig. 18). It can be seen that the *B-H* loops for the DC-plated sample and the sample plated with t_{forward} = 3760 ms are very similar, i.e., both have a high coercivity and consist of three regions, which, as previously mentioned, is typical of out-of-plane anisotropy.

The *B-H* loop for the sample-plated t_{forward} = 1200 ms is radically different with a very low coercivity, a two-region *B-H* loop, and a pronounced in-plane anisotropy.

Figure 19 shows the coercivity plotted against the forward on time for the two experimental runs.

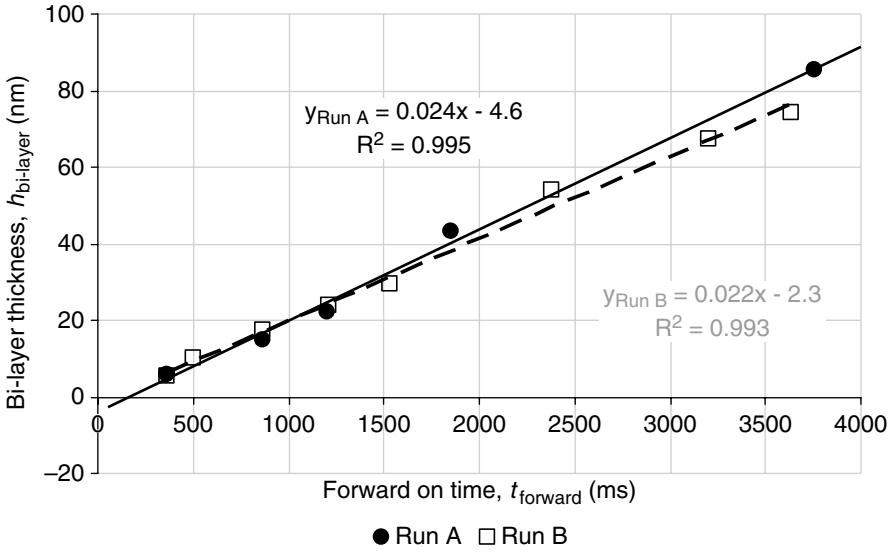

Fig. 17 Bi-layer thickness versus forward on time (Reproduced from McCloskey et al. [41])

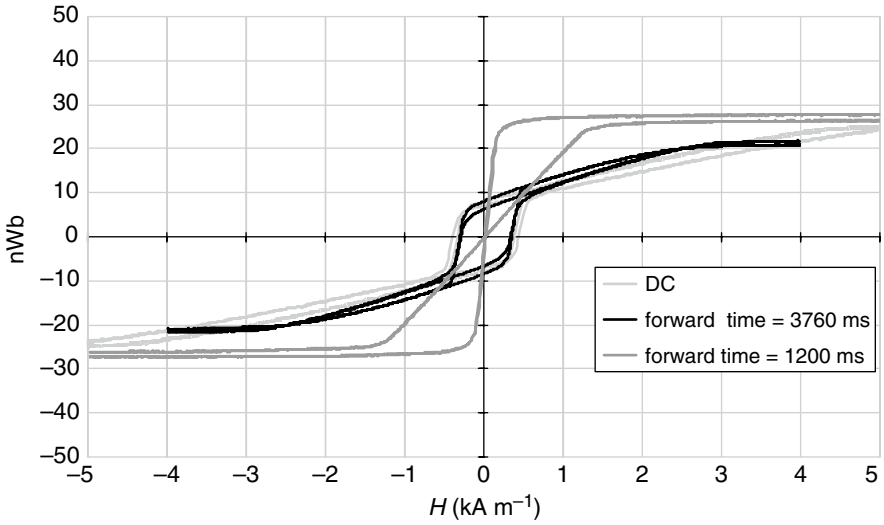

Fig. 18 Magnetisation plot for various values of forward on time

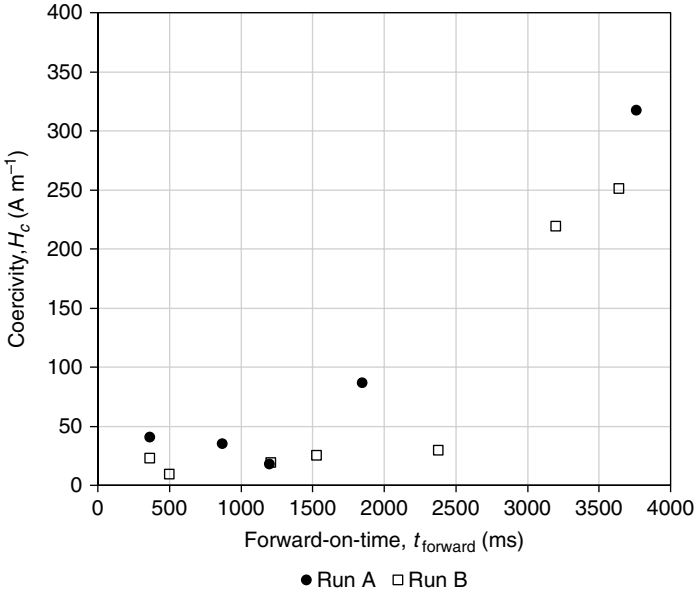

Fig. 19 Coercivity, H_c versus Forward On-Time, t_{forward} (Reproduced from McCloskey et al. [41])

Thus, for good soft magnetic properties, it is essential to use forward on times of 1530 ms or less. From Fig. 17, it can be seen that this corresponds to a bilayer thickness of 29 nm or less.

The relative permeability of the samples was found to be approximately 700 and was found to retain 90 % of its initial value to frequencies of up to 103 MHz. The anisotropy field was found to vary between 1.2 and 1.5 kA m^{-1} with the higher values being obtained at lower phosphorus contents.

The resistivity of the samples varied between 1.16×10^{-6} Ω m at 13 at.% P and 1.36×10^{-6} Ω m at 17 at.% P.

Electrodeposited Co-P with Improved Temperature Stability

Background

Electrodeposited amorphous Co-P is an attractive material for use in the integration of on-chip inductors into silicon process technology because of its high resistivity and advantageous magnetic properties. However, as it is an amorphous material, the properties of Co-P are dramatically changed upon crystallization. The stability of magnetic properties with respect to temperature is important since in fabricating an integrated inductor the magnetic core is likely to be exposed to processes such as the thermal cure of polymeric photoresist used to provide electrical insulation. A good candidate material is the Cyclotene 3000 series from Dow, which is derived from B-staged bisbenzocyclobutene (BCB) monomers. These materials use a soft cure temperature of 210 °C and hard cure temperatures of 250 °C and 300 °C [42].

This section concerns work undertaken to evaluate the inclusion of rhenium in a cobalt–phosphorus amorphous alloy in order to improve its thermal stability.

Oda et al. [43] used small additions of tungsten to improve crystallization temperature of amorphous Fe-Co-P alloys. Tungsten has a large atomic weight of 183.8 g $mol^{-1}$and it is thought that its large atomic radii play a role in bringing about an increase in crystallization temperature. However, despite extensive experimental trials, it was found that Co-P electroplating baths containing tungsten were found to have a considerable tendency to be unstable and a reliable plating bath for the deposition of Co-P-W was not identified.

Rhenium also has a large atomic weight of 186.2, and Brenner [39] describes how it can be readily codeposited with iron group metals. Hence, it was decided to determine if the inclusion of rhenium in Co-P was feasible and if its presence did in fact improve the thermal stability of the new composition. Finally, the effect of including Re on properties other than thermal stability was also investigated.

Experimental

A plating bath was prepared with a composition (see Table 3) very similar to that used by Riveiro and Riveiro [12], apart from the addition of $KReO_4$, which was used as the source of Re.

A glass beaker was used as the plating cell with a total solution volume of 1 l and agitation provided by mechanical stirring. The electrodes were horizontally

Table 3 Plating bath composition for Co-P-Re (Reproduced from McCloskey et al. [44])

Component	Amount (g l^{-1})
H_3PO_3	65
Co CO_3	39.4
$CoCl_2.6\ H_2O$	181
H_3PO_4	50
$KReO_4$	0–6

opposed, and the cathode-to-anode separation was 65 mm. The temperature of the solution was maintained at 72 °C using a hotplate and the plating carried out in "the presence of a uniaxial magnetic field of around 16 kA m^{-1} oriented to be parallel to the surface of the cathode. Cobalt metal pieces, in close contact with an inert Pt/Ti mesh, were used as the anode.

Copper foil with a thickness of 10 μm was used as a cathode to provide samples for annealing and DSC experiments. Silicon wafers with a top layer of 500 nm of oxide and a conductive sputtered seed layer consisting of 20 nm titanium and 200 nm copper was used as a substrate to provide samples for resistivity, permeability, and saturation magnetization measurement.

In all cases, the pulse reverse plating was used with parameters at values found to be optimal for Co-P plating [41]:

- Forward on time $t_{forward}$ = 860 ms
- Forward current density $CD_{forward}$ = 1520 A m^{-2}
- Reverse on time $t_{reverse}$ = 52 ms
- Reverse current density $CD_{reverse}$ = 620 A m^{-2}
- Off time t_{off} = 80 ms

As described earlier, the control of pH is very important in the plating of Co-P alloys since at higher values of pH, plating of nonmetallic deposits can occur with an adverse effect on the coercivity of the as-deposited film. Furthermore (and described in detail later), it was found that the temperature stability of the deposit is adversely affected by low pH conditions. Consequently, the pH was adjusted by addition of either HCl or NaOH.

DSC analysis using a Perkin Elmer Pyris 1 instrument was carried out on free-standing samples that were produced by dissolving the underlying copper foil. An aqueous 30 g l^{-1} ammonium persulfate, $(NH_4)_2S_2O_8$ at 40 °C was used as the etchant to remove the Cu foil.

Results and Discussion

Composition Analysis

The composition of Co-P and Co-P-Re samples plated on Cu foil is shown in Fig. 20.

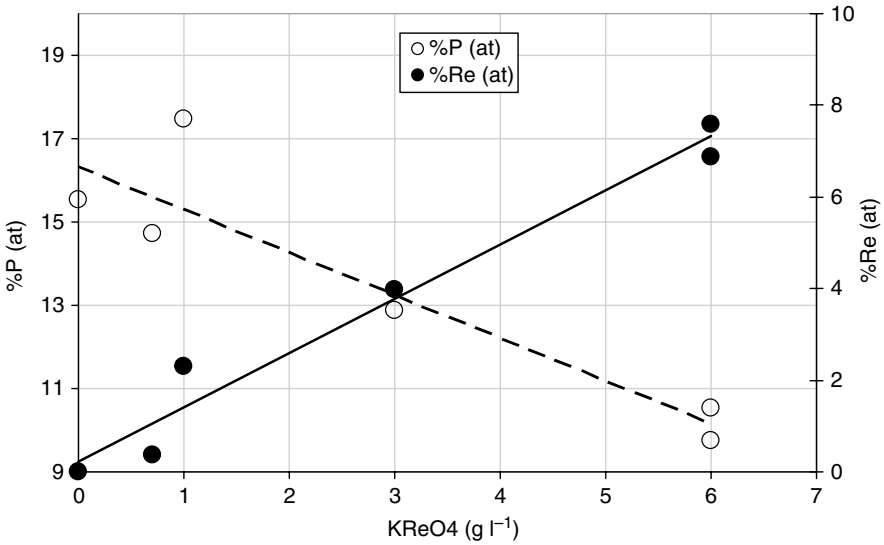

Fig. 20 Composition of Co-P and Co-P-Re samples (Reproduced from McCloskey et al. [44])

It can be seen that as expected increasing the amount of $KReO_4$ led to an increase in the amount of Re in the plated film. However, increasing the amount of $KReO_4$ in the bath also led to a dramatic reduction in the amount of P in the plated film.

Thermal Annealing

Thermal annealing experiments were carried out under vacuum and consisted of a 15 min ramp, a 30 min dwell at the peak temperature of 298 °C, and approximately 20 min cooling. Prior to the annealing, all the samples showed coercivity $H_c < 120$ A m^{-1}.

The coercivity of samples after a thermal annealing at 298 °C for 30 min plotted against pH is shown in Fig. 21.

It can be observed that the pH of the bath had a very strong effect on the coercivity values obtained after annealing. However, the coercivity of the Co-P samples produced at higher pH values was still very high.

Figure 22 shows hard axis hysteresis loops obtained before (as plated) and after a 298 °C anneal for a Co-P sample produced with a pH value of 0.79. The dramatic affect of the 298 °C annealing on the B-H loop of the sample can be seen with the coercivity increasing from 80 A m^{-1} to 1.9 kA m^{-1}.

In contrast, as can be seen in Fig. 21, the samples produced with a $KReO_4$ addition all had coercivity values after annealing that were significantly lower than similar Co-P samples. Furthermore, very low coercivity values $H_c < 80$ A m^{-1} were obtained for samples with an addition of 3 g l^{-1} or more of $KReO_4$.

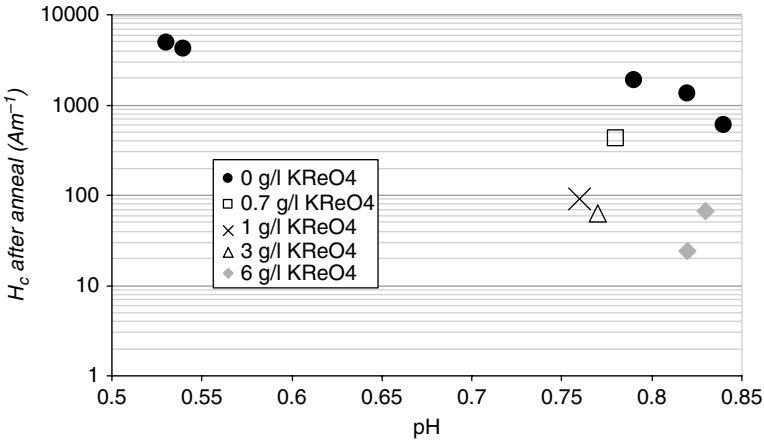

Fig. 21 Coercivity after thermal annealing at 298 °C for 30 min plotted against pH

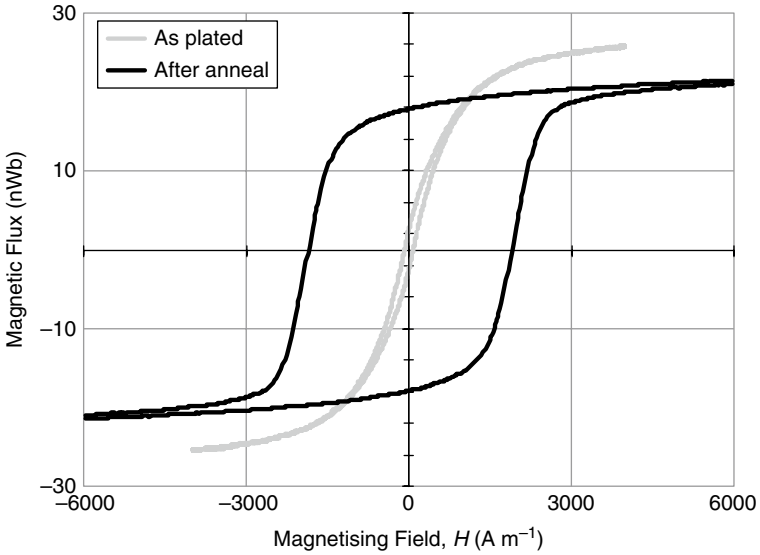

Fig. 22 Hysteresis loops before and after a 298 °C anneal for a Co-P sample produced with a pH value of 0.79 (Reproduced from McCloskey et al. [44])

The hard-axis hysteresis loops obtained before (as plated) and after 298 °C annealing for a Co-P-Re sample produced with 1 g l^{-1} $KReO_4$ and at a pH value of 0.76 are shown in Fig. 23.

It can be seen that the B-H loop for the Co-P-Re sample is largely unaffected by the 298 °C anneal with the coercivity $Hc < 80$ Am^{-1} after annealing.

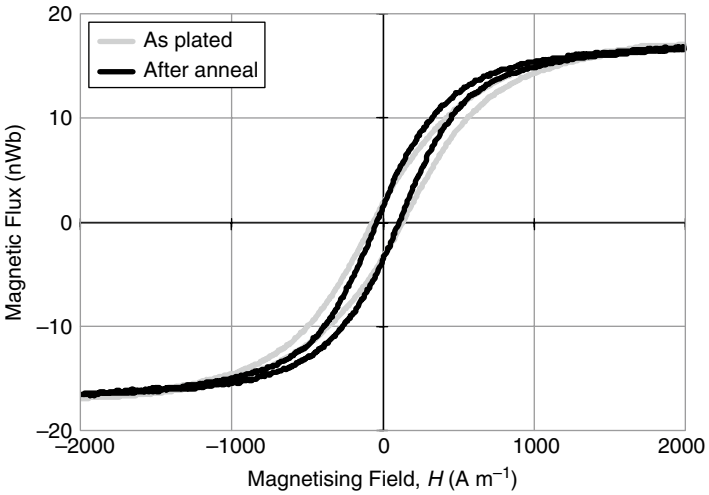

Fig. 23 Hysteresis loops before and after a 298 °C anneal for a Co-P-Re sample (Reproduced from McCloskey et al. [44])

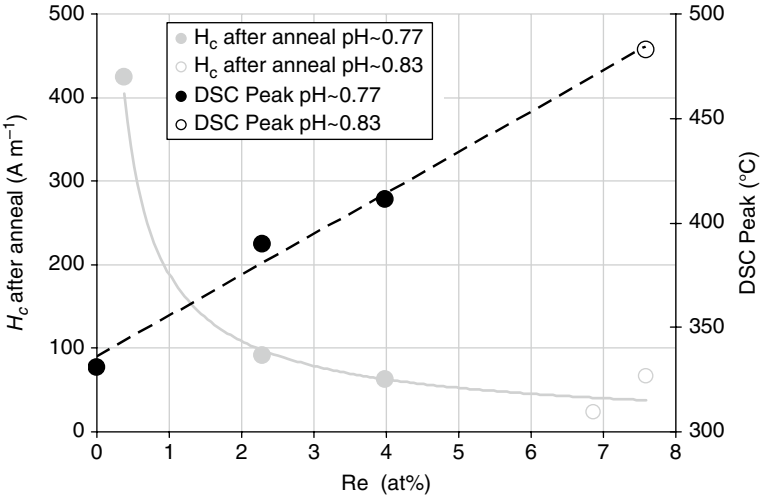

Fig. 24 DSC Peak and Coercivity (H_c) for Co-P-Re after 298 ^{O}C annealing for 30 min

Differential Scanning Calorimetery (DSC) analysis

The DSC analysis was carried out using a Perkin Elmer Pyris 1 instrument with a scan rate of 10 °C/min. The phase change peak from the DSC analysis and the coercivity after a 298 °C anneal for the a-Co-P-Re samples are shown in Fig. 24.

The pH of the bath was maintained in the range 0.76–0.83, and in fact four of the samples were produced at a pH ~ 0.77 while two were produced at a pH ~ 0.83.

Separate plots of H_c and DSC peak versus at.% Re are shown for each of these pH values. Again as discussed previously, prior to annealing, H_c <120 A m^{-1} for all the samples, and it can be seen that for all the samples with Re > 2 at.%, the coercivity after thermal treatment remains very low. It can also be seen that the trend line for H_c after annealing is the same for both pH values and hence it appears that the effect of the higher pH is effectively eliminated at the higher at.% Re values.

It can also be observed that the DSC peak increases sharply with increasing at.% Re. Again, it can be seen that the trend line is the same for both values of pH and hence pH had little effect.

Saturation Magnetization and Resistivity

The saturation magnetization (B_s) and resistivity (ρ) for Co-P and Co-P-Re samples plated on a silicon substrate are shown in Figs. 25 and 26 respectively.

It can be seen that apart from one sample (with Co = 82.4 at.%) the B_s values obtained for higher values of Re (Re > 3 at.%) are reasonably consistent with those obtained for lower values (Re < 3 at.%). Moreover, the sample with 82.4 at.% Co had a Re content of 3.1 at.%, and hence it does not appear that the lower-than-expected value of B_s obtained arose from its Re content.

It would be expected that the resistivity value obtained should be lower at lower values of P content. However, the dependence of P content on the Re content shown in Fig. 20 means that samples with a high Re content (Re > 3 at.%) also tended to have lower levels of P than those with a low Re content (Re < 3 at.%). Contrary to this, the resistivity of the samples does not seem to have been dramatically affected by the level of Re. This is probably due to the difference in the value of resistivity between Re ($\rho = 18 \times 10^{-8}$ Ω m) and Co ($\rho = 6 \times 10^{-8}$ Ω m).

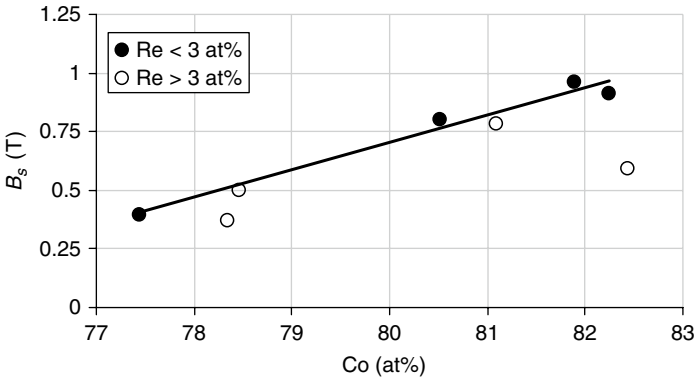

Fig. 25 Saturation Magnetisation (B_s) for as plated Co-P and Co-P-Re (Reproduced from McCloskey et al. [44])

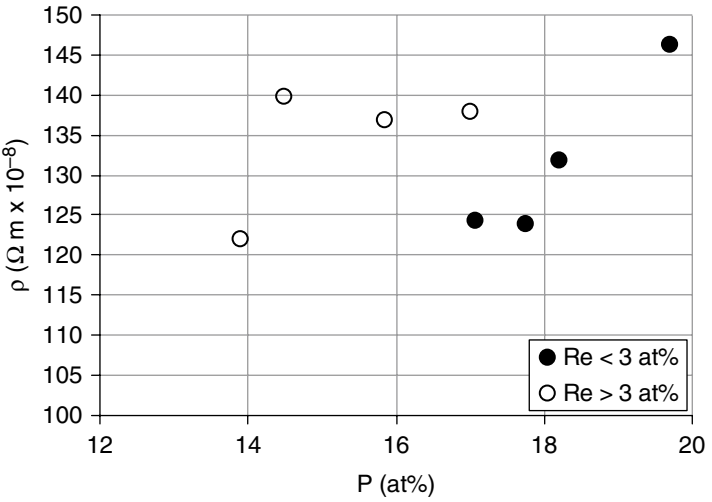

Fig. 26 Resistivity for as plated Co-P and Co-P-Re (Reproduced from McCloskey et al. [44])

Conclusions

Plated multi-nanolayer Co-P films were produced that show a higher saturation magnetization B_s in the range of 0.9–1.2 T and good soft magnetic properties, typically H_c < 40 A m^{-1} with a minimum value of 8 A m^{-1}. The films had an anisotropy field between 1.2 and 1.5 kA m^{-1} and resistivity in the range of 1.16×10^{-6} to 1.36×10^{-6} Ω m.

An electrodeposited magnetic alloy, Co-P-Re, was obtained that shows a significantly improved thermal performance in comparison to Co-P, retaining H_c < 120 A m^{-1} after a thermal annealing under vacuum at 298 °C for 30 min. These results were obtained for alloys with a composition of $Co_{100-x-y}P_xRe_y$, where 9.7 at.% < x < 17.5 at.% and 2.3 at.% < y < 7.6 at.%. It was found that other important properties, i.e., B_s and ρ, were largely unaffected by the addition of Re.

References

1. Karkare M (2008) Nanotechnology: fundamentals and applications. I. K International, New Delhi
2. Hanrahan JP, Copley MP, Ziegler KJ, Spalding TR, Morris MA, Steytler DC, Heenan RK, Schweins R, Holmes JD (2005) Pore size engineering in mesoporous silicas using supercritical CO_2. Langmuir 21:4163
3. Mansoori G (2005) Principles of nanotechnology. World Scientific, Hackensack
4. Wilson M, Kannangara K, Smith G, Simmons M, Raguse B (2002) Nanotechnology: basic science and emerging technologies. CRC Press LLC, Boca Raton, Florida

5. Lacaze PC (2013) Nanotechnologies: concepts, processing and applications. Wiley, Hoboken
6. Moore GE (1965) Cramming more components onto integrated circuits. Electronics 114–117
7. Roco MC, Gargini P (2011) Nanoelectronics: an international perspective. Proc IEEE 99:751
8. Information Storage Industry Consortium (2011) International magnetic tape storage roadmap, © Information Storage Industry Consortium, http://www.insic.org/news/A&S%20Roadmap.pdf
9. Wolf SA, Awschalom DD, Buhrman RA, Daughton JM, von Molnár S, Roukes ML, Chtchelkanova AY, Treger DM (2001) Spintronics: a spin-based electronics vision for the future. Science 294:1488–1495
10. Bird KD, Schlesinger M (1995) Giant magnetoresistance in electrodeposited Ni/Cu and Co/Cu multilayers. J Electrochem Soc 142:L65–L66
11. Simunovich D, Schlesinger M, Snyder D (1994) Electrochemically layered copper-nickel nanocomposites with enhanced hardness electrochemical society letters. J Electrochem Soc 141(1): L10–L11, doi:10.1149/1.2054717
12. Riveiro JM, Riveiro G (1981) Multilayered magnetic amorphous Co-P films. IEEE Trans Magn MAG 17(6):3082
13. Pérez L, de Abril O, Sánchez MC, Aroca C, López E, Sánchez P (2000) Electrodeposited amorphous CoP multilayers with high permeability. J Magn Magn Mater 215–216:337–339
14. Paunovic M, Schlesinger M, Snyder DD, Paunovic M (2010) Chapter 1, "Fundamental considerations". In: Schlesinger M, Paunovic M (eds) Modern electroplating, 5th edn. Wiley
15. Alper M, Aplin PS, Attenborough K, Dingley DJ, Hart R, Lane SJ, Lashmore DS, Schwarzacher W (1993) Growth and characterization of electrodeposited Cu/Cu-Ni-Co alloy superlattices. J Magn Magn Mater 126(1–3):8–11
16. Yahalom A, Tessier DF, Timsit RM, Rosenfeld AM, Mitchel DF, Robinson PT (1989) J Mater Res 4/4:755
17. Attenborough K, Hart R, Lane SJ, Alper M, Schwarzacher W (1995) Magnetoresistance in electrodeposited Ni-Fe-Cu/Cu multilayers. J Magn Magn Mater 148:335–336
18. Landolt D (1994) Electrochemical and materials science aspects of alooy deposition. Electrocimica Acta 39(8/9):1075–1090
19. Djokic SS (1999) Electrodeposition of Amorphous Alloys Based on the Iron Group of Metals 146(5):1824–1828
20. Brenner A, Couch DE, Williams EK (1950) Electrodeposition of alloys of phosphorous with nickel or cobalt. J Res Natl Bur Stand 44:109
21. Dekker AJ (1957) Solid state physics. Prentice-Hall, Englewood
22. Cullity BD (1972) Magnetic materials. CRC Press LLC, Boca Raton, Florida
23. Weiss P (1906) La variation du ferromagnetisme du temperature. Compte Rendu 143: 1136–1139
24. Cuillity BD, Graham CD (2009) Introduction to magnetic materials, 2nd edn. Wiley, IEEE Press
25. Roozeboom F, Bloemen PJH, Klaassens W, Van De Riet' EGJ, Donkers JJTM (1998) Soft-magnetic fluxguide materials. Philips J Res 51:59–91
26. Riveiro JM, Sanchez-Trjillo MC (1980) Magnetic anisotropy of electrodeposited Co-P amorphous alloys. IEEE Trans Magn MAG-16(6):1426–1428
27. Néel L (1949) Théorie du trainage magnetique desferromagnetiques engrains fins avec applications aux terres cuites 5:99
28. Papaefthymiou GC (2009) Nanoparticle Magnetism. Nano Today 4:438
29. Jones RE Jr (1990) IBM Disk Storage Tech 3:6
30. Tsang C, Chon M-M, Yogi T, Ju K (1990) Gigabit density recording using dual-element MR/inductive heads on thin-film disks. IEEE Trans Magn MAG-26:1689
31. Robertson N, Hu HL, Tsang C (1997) High performance write head using NiFe 45/55. IEEE Trans Magn 33:2818
32. Harada K, Takahashi F (1997) Nikkei Electron 691:91
33. Osaka T, Takai M, Tachibana H (2000) US Patent 6,063,512
34. Riveiro JM, Sanchez MC, Riveiro G (1981) Electrodeposited Co-P alloys with variable magnetic anisotropy. IEEE Trans Magn MAG 17(3):1282–1285

35. Gardner DS et al (2006) IEEE International Electron Device Meeting (IEDM), San Francisco, pp 11–13
36. Chi GC, Cargill GS III (1975) Structural anisotropy of amorphous cobalt-phosphorus alloys. AIP Conf Proc 29:147
37. Ruythooren W, De Boeck J, Celis JP (2004) Microstructural investigation of Co-P by TEM. J Electrochem Soc 151(5):C315–C317
38. Perez L, Aroca C, Sánchez P, López E, Sánchez MC (2004) Planar fluxgate sensor with an electrodeposited amorphous core. Sens Actuators A 109:208–211
39. Brenner A (1963) Electrodeposition of alloys. Academic, London
40. Riveiro JM, Guijarro MS, Rivero G, Sánchez MC (1982) Magnetic domains in multilayered amorphous Co-P alloys. Phys Rev D 15:145
41. McCloskey P, Jamieson B, O'Donnell T, Gardner D, Morris MA, Roy S (2008) High-frequency nanostructured magnetic materials for integrated inductors. J Magn Magn Mater 320(20): 2509–2512
42. Wang H, Yi X, Chen S, He S, Xiaochao F, Ma H (2006) Planarization of CMOS ROIC dies for uncooled detectors. Infrared Phys Technol 47:251–256
43. Oda M, Ohashi H, Kamadu K (1995) US Patent 5,435,903
44. McCloskey P, Jamieson B, O'Donnell T, Gardner D, Morris MA, Roy S (2010) Electrodeposited amorphous Co-P based alloy with improved thermal stability. J Magn Magn Mater 322(9–12): 1536–1539